Boat-shaped Buoy Optimization of an Ocean Wave Energy Converter Using Neural Networks and Genetic Algorithms

Weihan Lin

Thesis submitted to the Faculty of the

Virginia Polytechnic Institute and State University

in partial fulfillment of the requirements for the degree of

Master of Science

in

Mechanical Engineering

Lei Zuo, Chair

Danesh Tafti

Pinar Acar

May 09, 2022

Blacksburg, Virginia

Keywords: Renewable Energy Generation, Wave Energy Converter, Neural Network, Genetic Algorithm, Optimization

Boat-shaped Buoy Optimization of an Ocean Wave Energy Converter Using Neural Networks and Genetic Algorithms

Weihan Lin

(ABSTRACT)

The point absorber is one of the most popular types of ocean wave energy converter (WEC) that harvests energy from the ocean. Often such a WEC is deployed in an ocean location with tidal currents or ocean streams, or serves as a mobile platform to power the blue economy. The shape of the floating body, or buoy, of the point absorber type WEC, is important for the wave energy capture ratio and for the current drag force. In this work, a new approach to optimize the shape of the point absorber buoy is developed to reduce the ocean current drag force on the buoy while capturing more energy from ocean waves. A specific parametric modeling is constructed to define the shape of the buoy with 12 parameters. The implementation of neural networks significantly reduces the computational time compared to solving hydrodynamics equations for each iteration. And the optimal shape of the buoy is solved using a genetic algorithm with multiple self-defined functions. The final optimal shape of the buoy in a case study reduces 68.7% of current drag force compared to a cylinder-shaped buoy, while maintaining the same level of energy capture ratio from ocean waves. The method presented in this work has the capability to define and optimize a complex buoy shape, and solve for a multi-objective optimization problem.

Boat-shaped Buoy Optimization of an Ocean Wave Energy Converter Using Neural Networks and Genetic Algorithms

Weihan Lin

(GENERAL AUDIENCE ABSTRACT)

The marine kinetic energy includes ocean waves power, tidal power, ocean current power, ocean thermal power and river power. The total potential marine kinetic energy in 2021 is 2300 TWh/year, where 1400 TWh/year is from the ocean wave power. To discover and harvest the huge potential power from the marine, researchers have been developed for different types of WECs for several decades. One of the most successful concepts is the point absorber typed WEC, which can extract waver energy from the heaving vibration motion of a floating body and convert the kinetic energy into electrical energy. This thesis presents an optimization strategy to optimize the shape of the floating body to improve power extraction and reduce the installation cost by implementing the machine learning tool and genetic algorithm. Compared with the state-of-the-art optimization strategies, the proposed optimization method allows the floating body to have more parameters in shape changes and reduces the computational cost from minutes to milliseconds. The final optimized floating body shape performs extraordinarily compared to the other two state-of-the-art floating body shapes.

Dedication

This study is heartfeltly dedicated to my loving parents, Mr. Yinhai Lin and Mrs. Guilian Lv, for their endless love and support, to my friends in real life and online for their kindly accompany and care.

Acknowledgments

I would like express my deepest appreciation to my advisor, Prof. Lei Zuo, for his valuable guidance and support, and to my committee members, Prof. Danesh Tafti and Prof. Pinar Acar for their valuable suggestions. Without their knowledge and advice, this study wouldn't be able to this deep.

I would like to thank the partial financial support from the Office of Naval Research (ONR) with grant # N00014-21-1-2152.

I would like to thank my lab mates: Xiaofan Li, Belal Hassan Shanab, Corbin Lenderink, Xian Wu, Jianuo Huang, Lisheng Yang, Jia Mi, Kan Sun, Jiajun Zhang, Feng Qian, Mingyi Liu, Shuo Chen, Boxi Jiang, Qiaofeng Li, Bonan Qin, Yuzhe Chen, Qiuchi Xiong, Vishnu Vijayasankar, Hongjip Kim for the help on my research work and technical discussions.

Contents

List of Figures

List of Tables

Chapter 1

Introduction

1.1 Marine Energy

Marine and hydrokinetic (MHK) energy, one of the largest renewable energy resources, has been studied extensively by many researchers in the past few decades. In 2021, an U.S. government report from the National Renewable Energy Lab mentioned that the technically-achievable power potential of U.S. marine energy resources could reach to 2300 TWh/year, including 1400 TWh/year of wave energy and 269 TWh/year of tidal and current energy [1].

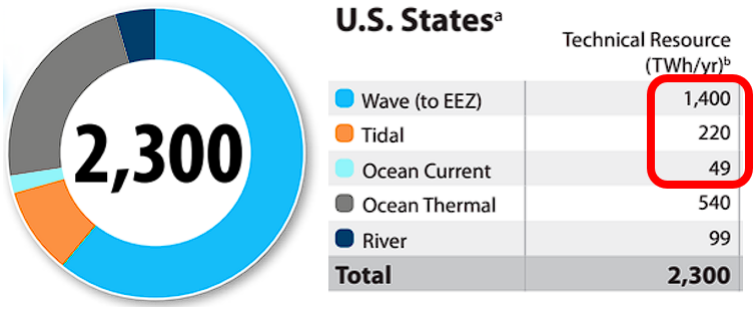

Figure 1.1: Technical Power Potential of U.S.Marine Energy Resources (in TWh/year)[1]

In addition, the deployment of the MHK can complement with other forms of renewable energy such as wind [10] and solar [11] and benefit from it. Because of the huge potential of marine energy, researchers have made many attempts on designing and optimizing different types of devices to convert marine energy into electricity [12]. Qiao indicated that only for wave energy converter (WEC), more than 1000 prototypes have been developed [13].

These various types of WECs can be categorized based on different criteria, for example, Falcao divided all WECs into three subcategories, which are the Oscillating Water Column (OWC), oscillating body device, and the overtopping device [2]. Many are already verified. For example, the Voith Hydro Wavegen has a record of operating for 60,000 hours with their OWC [14]. The Oceanlinx MK3 floating OWC is verified through offshore testing [2]. The Pelamis WEC with a hydraulic PTO designed by Herdenson is tested through a 1/7 scale prototype and proved the high efficiency of the PTO [15]. Elwood et al. designed a two-body point absorber with a linear generator and tested it at Yaquina Bay in Oregon state [16]. The Wave Dragon WEC with hydro turbines as power take-off (PTO) is tested offshore in Denmark and connected to the grid [17]. Beyond the above mentioned projects, many other prototypes are developed and tested in the ocean, which includes the Wavebob [18], PowerBuoy [19], Oyster [20], RME [21], Lifesaver [22], Calwave [23], etc.

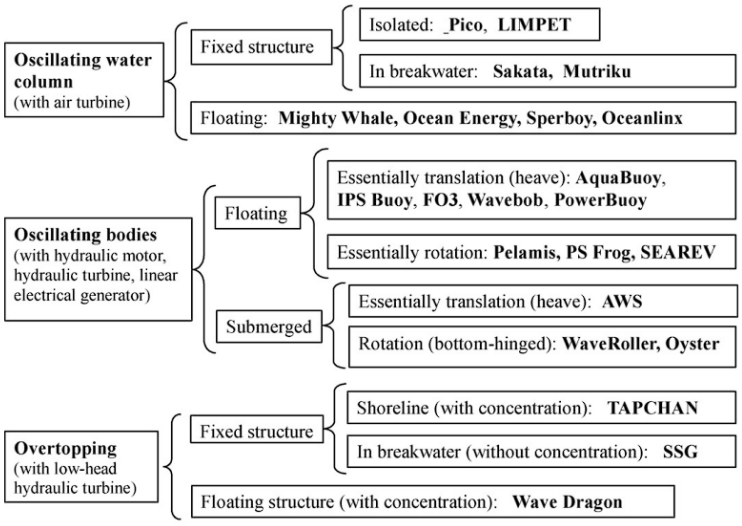

Figure 1.2: Different types of WECs [2]

1.2 Point Absorber Optimization

Among all the prototypes, point absorber is one of the major types, which harvests the wave energy with a power take-off system from the relative motion between the floating or submerged buoy and a fixed or oscillating reference [24].

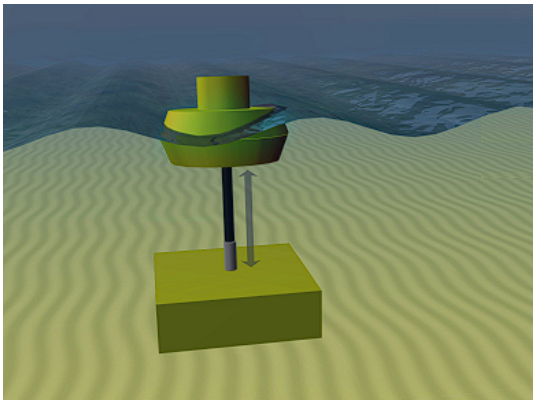

Figure 1.3: A simple point absorber typed WEC structure [3]

In 1970s, Budal and Falnes proposed the idea of absorbing wave energy through a floating buoy and analyzed the optimum condition for it [25][26]. Many researchers soon followed on the topic and generated many branches on different aspects. For example, the hydrodynamic study which includes the analysis done by Mei et al. [27][28] and many other researchers [29]; the structure analysis including the work by Evans and Porter [30] and Martin et al. [31]; the PTO design and characterization like the work of Jiang et al [4], Sun et al. [32] and many other works [33]; the control algorithms development including the effort of Ringwood [34], Zou et al. [35], and Korde and Ringwood [36]. A lot of these topics made contributions on improving the performance of the point absorber.

Besides the above mentioned topics, many researchers have investigated the shape optimization of the point absorber buoys to further increase the power absorption from a single device [37]. Gilloteaux and Ringwood optimized the diameter and the draft (distance from

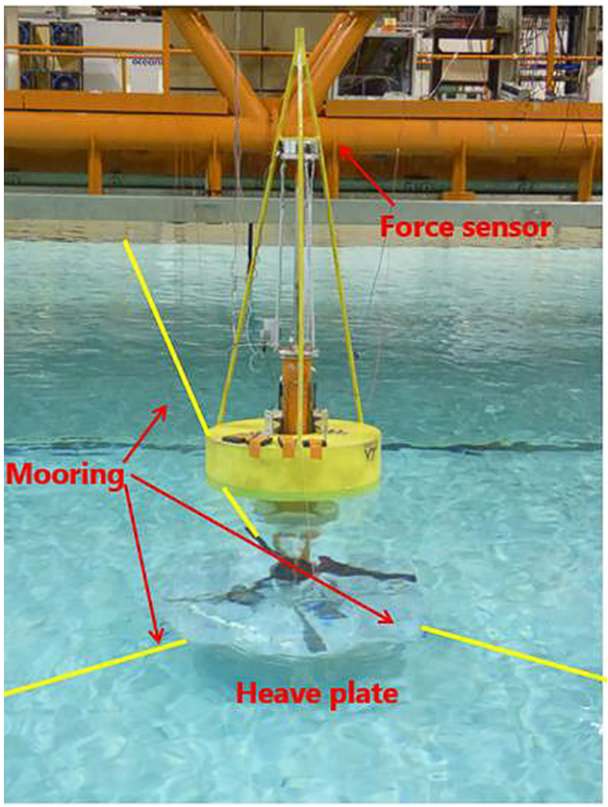

Figure 1.4: Point absorber in the tank test [4]

the waterline to the deepest point of the buoy) of a cylindrical buoy on a single body heaving point absorber [38]. De Backer investigated the hydrodynamic performance of a vertical cylinder buoy with conical bottom and spherical bottom on the point absorber, and found the optimal bottom shape and size with objective of maximizing the power absorption at a certain sea state [5]. Beirao and Malca evaluated the stress concentration and the induced displacement for spherical, cylindrical and tulip buoy on a point absorber and found that the spherical had the best structurec [39]. Edwards and Yue designed a framework for a single body point absorber that can significantly reduce the surface area and volume of the buoy [40].

The above mentioned buoy shape optimization of a point absorber were mostly restricted

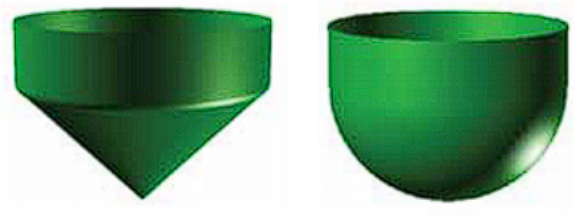

Figure 1.5: Some traditional optimized buoy shapes [5]

on a cylindrical, spherical, cone-based or other shapes of revolving buoy and the design parameters have typically included the diameter, the draft and the buoy shape type. The reason for choosing a body of revolution is that it can adapt to wave from any directions. However, this is only suitable for the point absorbers that are anchored at a fixed location. For the self-powered ocean observation platform proposed in this work, the current drag acting on the floating cylindrical buoy is large, which would add additional constraint to the shape optimization problem. Therefore, it is necessary to develop additional and more flexible buoy shapes that allow more parameters to be optimized under multiple constraints. Abdelkhalik et al. designed an axis-symmetric buoy using a polynomial and a Bézier curve with five control points for a single body heaving point absorber [6]. By changing the polynomial coefficients and the control points position, the paper built and discussed various buoy shapes and their energy extraction efficiency. However, the paper did not provide an optimal shape with this method due to difficulties associated with the computational time and geometry meshing for hydrodynamic simulations. Since computational complexity of hydrodynamic simulations increases as the number of parameters increased, a powerful tool is necessary to improve the computational efficiency to produce an optimal buoy shape.

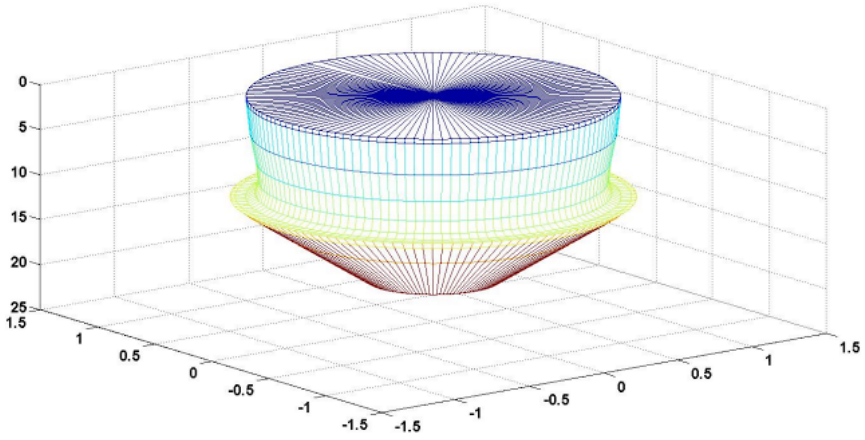

Figure 1.6: Optimized buoy shape using a Bézier curve [6]

1.3 Neural Networks and Genetic Algorithms (GA) in Marine Field

The neural networks and genetic algorithms (GA) have proved its worth in many studies in the ocean wave energy conversion. For example, Zhu et al. published a method using artificial neural networks and GA to optimize a wave energy converter array with 80% prediction accuracy [7]. Huang et al. designed a optimal power control method using a back propagation neural network and verified its advantage through experiment [41]. Li et al designed a real-time controller for an oscillation-body wave energy converter and studied the sensitivity and uncertainty of the energy conversion using an artificial neural network [8]. Bento et al. used the neural network to conduct short term wave prediction and achieved promising results [42].

The combination of neural network and GA is applied in the ship geometry optimization area as well. Abramowski developed a neural network model to estimate the effective power of the ship and then used GA to optimize the ship parameters including ship length, breadth,

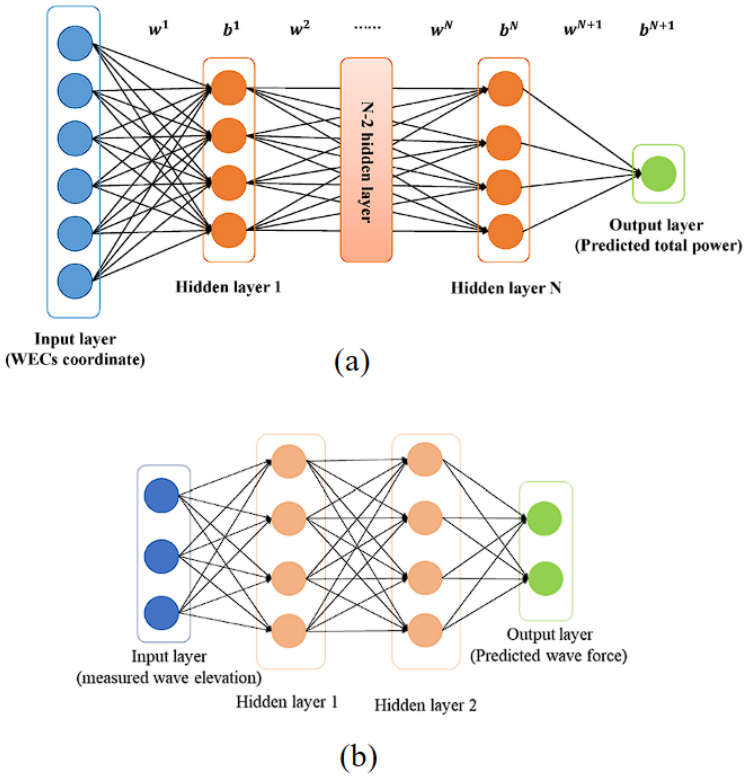

Figure 1.7: Some neural network structures used in the WECs field [7][8]

draught, block coefficient, waterplane coefficient and speed [43]. Shaeffer et al. optimized the ship hull of a rapid ship with design variables of the ship length, beam and fullness as shown in the Fig. 1.8 [9]. They started with a 'frigate' type hull form and discussed the performance of neural networks with different numbers of neurons and layers and found the final optimal hull shape. Cepowski used neural network to estimate the ship resistance by considering the ships length, breadth, draught and Froude number as input values, and the measured and estimated value difference was in a range of -1.2 to $+1.2$, which indicated a good performance of the developed neural network [44].

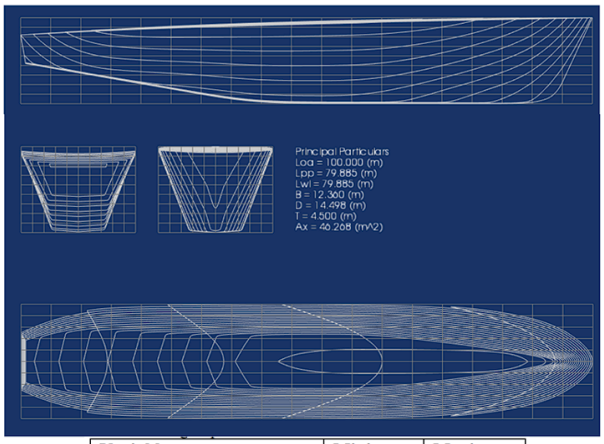

Variable	Minimum	Maximum
Length Overall (m)	100	200
Beam Overall (m)	20	25
Wetted Surface Area (m^2)*	2180	4880
Cb*	0.47	0.53
Cp*	0.63	0.70
Cwp*	0.78	0.86
Fullness Forward	0.10	0.75
Fullness Aft	0.10	0.75

Figure 1.8: Ship hull optimization [9]

1.4 Organization

The objective is to find the optimal buoy shape that captures the most wave energy while minimizing the current drag force. To achieve the goal, the thesis will develop a powerful parametric model using non-uniform rational b-splines that allows a more flexible shape of buoy. Additionally, a neural network will be build in this work to replace the traditional hydrodynamic simulation tool to reduce the computational complexity. Finally, a multi-objective optimization problem will be solved using a GA to search the optimal buoy shape.

The thesis is organized as follows. Chapter 2 introduces the methods of parametric modelling of the floating body; Chapter 3 constructs the heave motion dynamic modeling and current drag force modeling; Chapter 4 shows the implementation of the neural network; Chapter 5 presents the GA optimization results and compared the optimal shape to the state-of-arts buoy shapes. Chapter 6 concludes the work and indicate the future work.

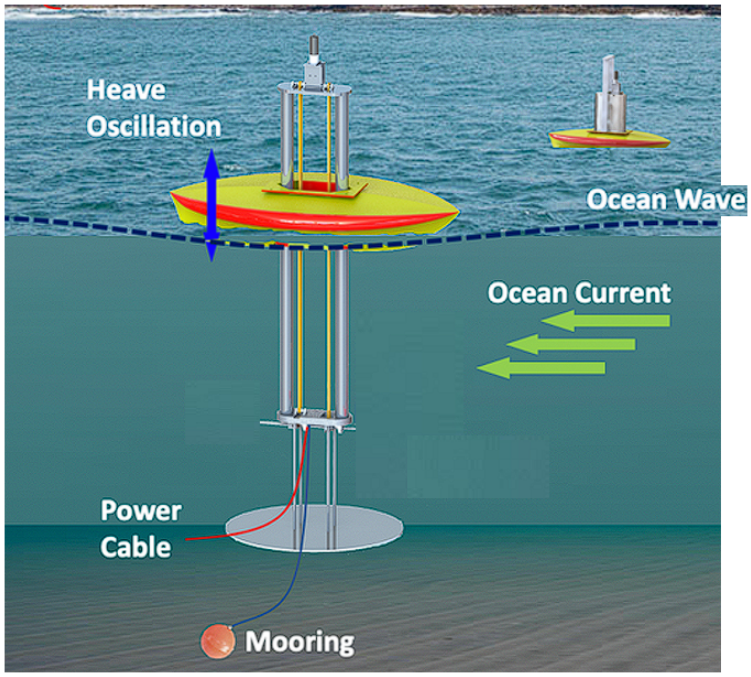

Figure 1.9: A simplified self-powered boat-shaped wave energy converter this thesis works on

Chapter 2

Parametric Modeling

In this Chapter, the parametric modeling of the floating buoy is introduced. In order to parameterize the shape of the buoy, this thesis applies non-uniform rational b-splines (NURBS) to the problem. By using the control points coordinates of the NURBS, the shape of the buoy can be represented as a vector of numbers, which is suitable and simple for future optimization.

2.1 Introduction of NURBS

NURBS is a mathematical representation of a geometry that can describe any curves or surfaces accurately. It is used in 3D modeling software, such as Solidworks, Rhinoceros, Autodesk Inventor, and etc. Because the geometry is built with NURBS that can be written as some mathematical equations, the information of the geometry that is required for rebuilding or transferring is significantly smaller than a mesh-based geometry. Moreover, it is more accurate comparing to the mesh-based geometry, because the mesh-based geometry will lose information when zooming in or out, while NURBS based geometry won't.

In order to understand NURBS, the Bézier curve is introduced first as shown in the following equations 2.1 and 2.3 [45]:

$$B_{i,0}(t) = \begin{cases} 1, & \text{if } t_i \leq t < t_{i+1} \\ 0, & \text{otherwise} \end{cases}$$
$$B_{i,d}(t) = \frac{t-t_i}{t_{i+d}-t_i} B_{i,d-1}(t) + \frac{t_{i+d+1}-t}{t_{i+d+1}-t_{i+1}} B_{i+1,d-1}(t) \tag{2.1}$$

$$B(t) = \sum_{i=0}^{n} B_{i,d}(t) p_i \tag{2.2}$$

where, $B_{i,d}(t)$ is the $i-th$ basis function of a b-spline with $d-th$ degree with parameter of t; p_i is the $i-th$ control point; t_i are the knots that form a knot vector $t = \{t_0, t_1, t_2, ..., t_m\}$; $B(t)$ is final the Bézier curve. The relationship between the degree d, number of control points $n+1$ and number of knots $m+1$ is given by $m = n+d+1$ [45].

Also, the first control point and the end control point are the end points of the curve, which means that:

$$\begin{cases} B_0 = B(0) \\ B_n = B(1) \end{cases} \tag{2.3}$$

Fig. 2.1 shows a linear Bézier curve $B(t)$ with control point of p_o and p_1 when $t = 0.3$. As t changes from 0 to 1, $B(t)$ describe the line connected by p_o and p_1.

The NURBS is similar to Bézier curve and the equation formulation is shown in 2.5:

$$N_{i,0}(u) = \begin{cases} 1, & \text{if } t_i \leq u < t_{i+1} \\ 0, & \text{otherwise} \end{cases}$$
$$N_{i,d}(u) = \frac{u-t_i}{t_{i+d}-t_i} N_{i,d-1}(u) + \frac{t_{i+d+1}-u}{t_{i+d+1}-t_{i+1}} N_{i+1,d-1}(u) \tag{2.4}$$

$$C(u) = \frac{\sum_{i=0}^{n-1} w_i N_{i,d}(u) p_i}{\sum_{i=0}^{n-1} w_i N_{i,d}(u)} \tag{2.5}$$

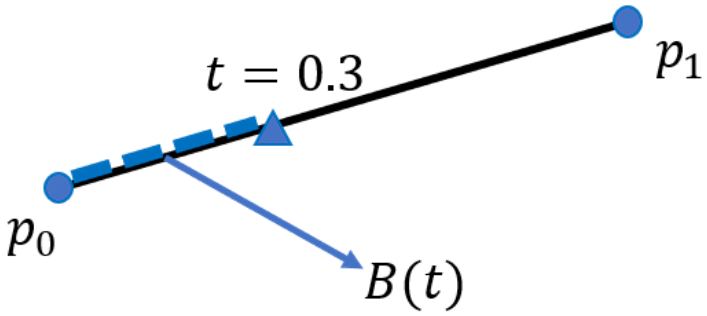

Figure 2.1: A linear Bézier curve $B(t)$ with control point of p_o and p_1 when $t = 0.3$

where, $N_{i,d}(u)$ is the $i-th$ basis function of a b-spline with $d-th$ degree with parameter of u; p_i is the $i-th$ control point; t_i are the knots that form a knot vector $U = \{t_0, t_1, t_2, ..., t_m\}$; $C(u)$ represent the formation of the NURBS. The relationship between the degree d, number of control points $n+1$ and number of knots $m+1$ is given by $m = n+d+1$ [45].

2.2 Modeling Using NURBS

To optimize the shape of the buoy, the shape should be parameterized so that it can be represented with a set of numbers to be suitable for a GA. The 3D model of the buoy was built in a commercial 3D modeling software, SOLIDWORKS. And the buoy model was constructed with one straight center-line and multiple cubic b-splines, including one outer-deck, one keel and several ribs as shown in Fig. 2.2. The parametric model consists of the coordinates of all b-spline control points. Considering that the aim is to have a more flexible buoy shape while not having too many parameters that increase the computational complexity, the b-spline control points of the outer-deck, keel and ribs are distributed regularly as shown in Fig. 2.3.

The 5 control points of the outer-deck, including 1 fixed vertex and 4 parameters (x_1, x_2,

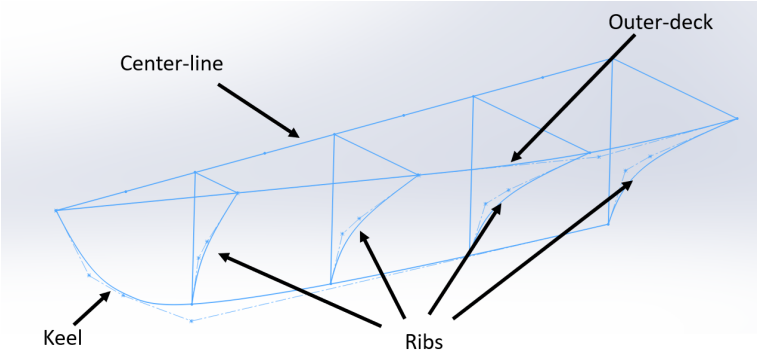

Figure 2.2: Construct a boat-shaped buoy using a straight center-line and multiple cubic b-splines, including one outer-deck, one keel and four ribs

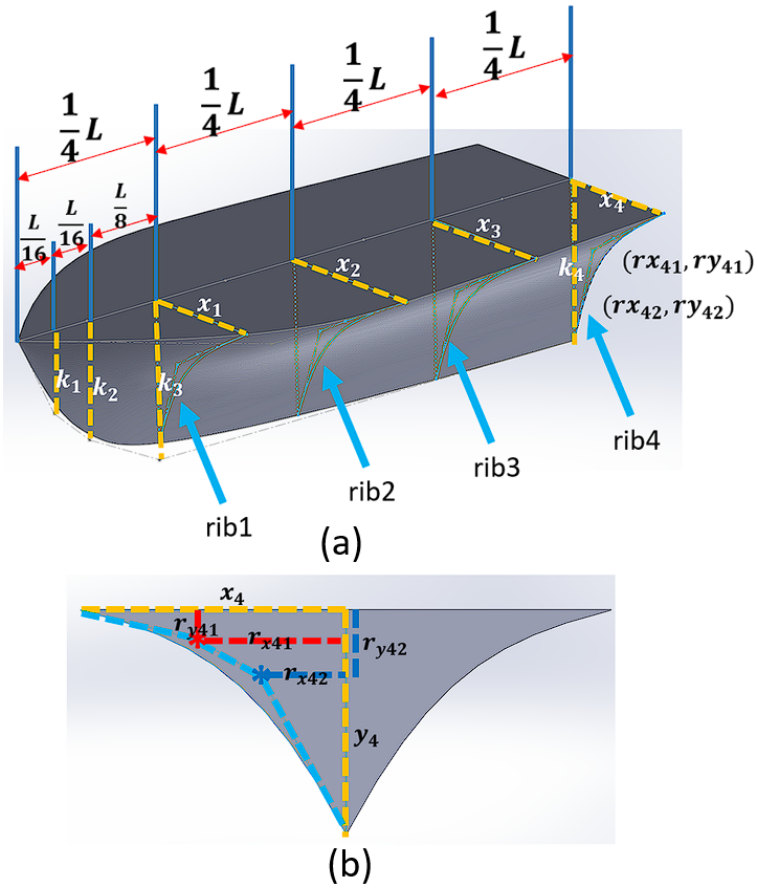

Figure 2.3: (a) All parameters that are required for the buoy shape parametric modeling; (b) Back view of the buoy and detailed information of rib parameters

x_3 and x_4), are evenly distributed along the center-line. The 5 control points of the keel, including 1 fixed vertex and 4 parameters (y_1, y_2, y_3 and y_4), are concentrated to the front, so that the geometry resembles a ship. Each rib is constructed with 4 control points, including 2 vertexes fixed by the outer-deck and keel and 4 parameters (r_{x41}, r_{x42}, r_{y41} and r_{y42}). However, to reduce the computational complexity, only "rib4" is parameterized. The rest of ribs are constructed by the same ratio, which is similar to the definition of similar triangle. For example, the coordinate of the top control point of "rib1" can be written as ($\frac{r_{x41}}{x_4}x_1$, $\frac{r_{y41}}{y_4}y_3$). Now the geometry can be represented as a vector s, where:

$$s = [x_1, x_2, x_3, x_4, y_1, y_2, y_3, y_4, r_{x41}, r_{x42}, r_{y41}, r_{y42}, L] \tag{2.6}$$

Since this study only considers optimizing the buoy with same length, the parameter vector can be further reduced to:

$$s = [s_x, s_y, s_r] \tag{2.7}$$

where,

$$\begin{aligned} s_x &= [x_1, x_2, x_3, x_4] \\ s_y &= [y_1, y_2, y_3, y_4] \\ s_r &= [r_{x41}, r_{x42}, r_{y41}, r_{y42}] \end{aligned} \tag{2.8}$$

2.3 Criteria and Constraints

Table 2.1 shows the dimension and the working condition of the targeting buoy of this study. To have a streamlined feasible deck-line and hull shape as mentioned in the work of Khan, Gunpinar and Dogan [46], constraints equations were developed in Eqn. (2.9) to (2.12) .

The shape parameter vector s must meet one of the 4 constraints equations to get a feasible

Table 2.1: Dimension and working condition of the target buoy

Properties	Values
Mass	$80kg$
Underwater volume	$0.08m^3$
Cross-sectional area at water level	0.5 - $0.6m^2$
Total length	$1.2m$
Maximum deck and keel length	$0.5m$
Minimum deck and keel length	$0.05m$
Current speed	$2m/s$
Wave period	$6sec$
Wave height	$0.5m$

$$
\begin{aligned}
&case1: \\
&s_i(j_1) <= s_i(j_1+1) \\
&where, \\
&i = \{x, y\}, \\
&j_1 = \{1, 2, 3\}
\end{aligned}
\tag{2.9}
$$

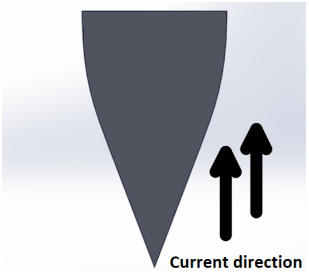

$$
\begin{aligned}
&case2: \\
&s_i(j_1) <= s_i(j_1+1) \\
&s_i(j_2) >= s_i(j_2+1) \\
&where, \\
&i = \{x, y\}, \\
&j_1 = \{1, 2\}, j_2 = \{3\}
\end{aligned}
\tag{2.10}
$$

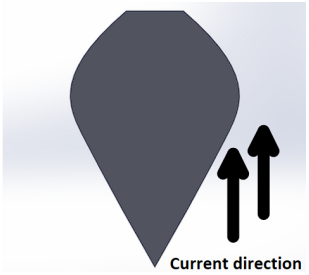

$$
\begin{aligned}
&case3: \\
&s_i(j_1) <= s_i(j_1+1) \\
&s_i(j_2) >= s_i(j_2+1) \\
&where, \\
&i = \{x, y\}, \\
&j_1 = \{1\}, j_2 = \{2, 3\}
\end{aligned}
\tag{2.11}
$$

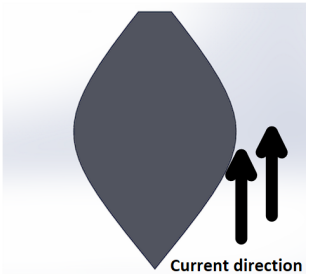

shape. Fig. 2.4 shows the differences between a boat-shaped buoy with a feasible deck line and one with an infeasible deck line.

$$
\begin{aligned}
&case4: \\
&s_i(j_1) >= s_i(j_1+1) \\
&where, \\
&i = \{x, y\}, \\
&j_1 = \{1, 2, 3\}
\end{aligned}
\tag{2.12}
$$

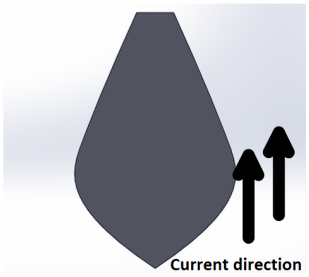

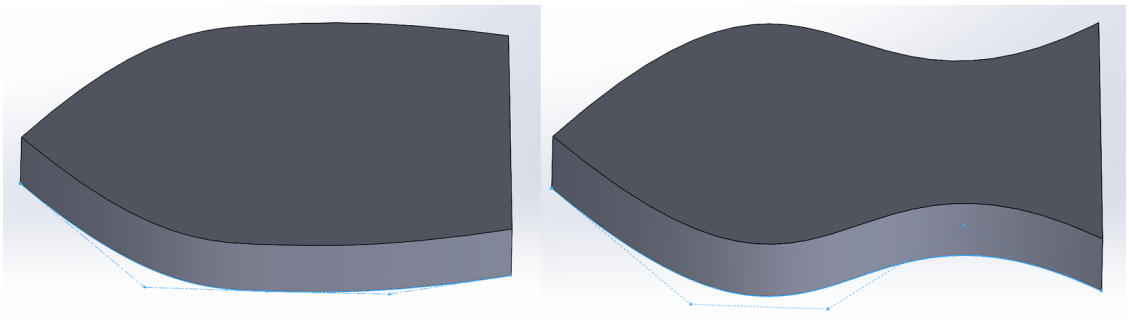

(a) Feasible deck line

(b) Infeasible deck line

Figure 2.4: (a) Desirable b-splines that form the deck line, keel and ribs. (b) Undesirable b-splines that form the deck line, keel and ribs.

Chapter 3

Dynamic Modeling

In this Chapter, the heave motion dynamic modeling and current drag force modeling is constructed to estimate the wave power extracted from heave direction and drag force from the surge direction. The Boundary Element Method (BEM) solver and Computational Fluid Dynamics (CFD) solver used for simulation in the Chapter includes Ansys AQWA and Ansys Fluent. The effects of mesh size in BEM and CFD solvers are discussed as well.

3.1 Heave Motion Dynamic Modeling

In this study, only heave and surge direction of motion is considered. Therefore, in order to calculate the wave power extraction on heave direction, the whole system can be treated as a two-body spring-mass-damper system as shown in the Fig. 3.1.

From the free body diagram, the equations of motion in frequency domain for the two-body point absorber system on heave motion is derived in Eqn. (3.1).

$$(-\omega^2 M + i\omega C + K)Z = F \tag{3.1}$$

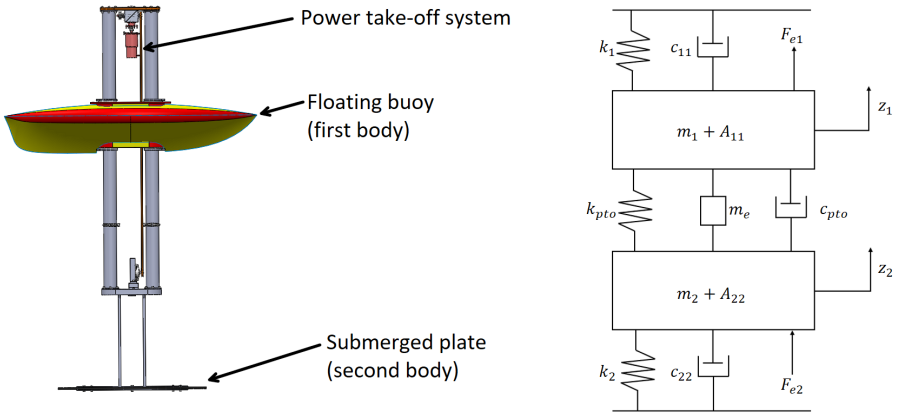

Figure 3.1: Free body diagram of the two-body point absorber system

And the matrix can be denoted by:

$$M = \begin{bmatrix} m_1 + A_{11} + m_e & -m_e \\ -m_e & m_2 + A_{22} + m_e \end{bmatrix} \tag{3.2}$$

$$C = \begin{bmatrix} c_{11} + c_{pto} & -c_{pto} \\ -c_{pto} & c_{22} + c_{pto} \end{bmatrix} \tag{3.3}$$

$$K = \begin{bmatrix} k_1 + k_{pto} & -k_{pto} \\ -k_{pto} & k_2 + k_{pto} \end{bmatrix} \tag{3.4}$$

$$F = \begin{bmatrix} F_{e1} \\ F_{e2} \end{bmatrix}, Z = \begin{bmatrix} z_1 \\ z_2 \end{bmatrix} \tag{3.5}$$

Here, m_1 and m_2 are the dry mass of the floating and submerged body, A_{11} and A_{22}, c_{11} and c_{22} are the frequency-dependent added mass and radiation damping of the floating and submerged body, k_1 and k_2 are the hydrostatic spring stiffness of the floating and submerged

body, F_{e1} and F_{e2} are the frequency-dependent excitation force of the floating and submerged body, m_e, c_{pto} and k_{pto} are the equivalent mass, damping coefficient and spring stiffness of the PTO. At regular wave condition, the equation can be solved for a closed form solution and the power absorbed from the heave motion can be expressed as:

$$P = \frac{1}{2}\omega^2 c_{pto}|Z_1 - Z_2|^2 \tag{3.6}$$

In order to get those frequency-dependent hydrodynamic parameters, a BEM solver is required for simulations. As shown in the Fig. 3.2, the environment setup of the BEM solver is a $15m \times 15m \times 20m$ $(Length \times Width \times Depth)$ large tank with four wave directions coming from $0°, 90°, 180°$ and $-90°$.

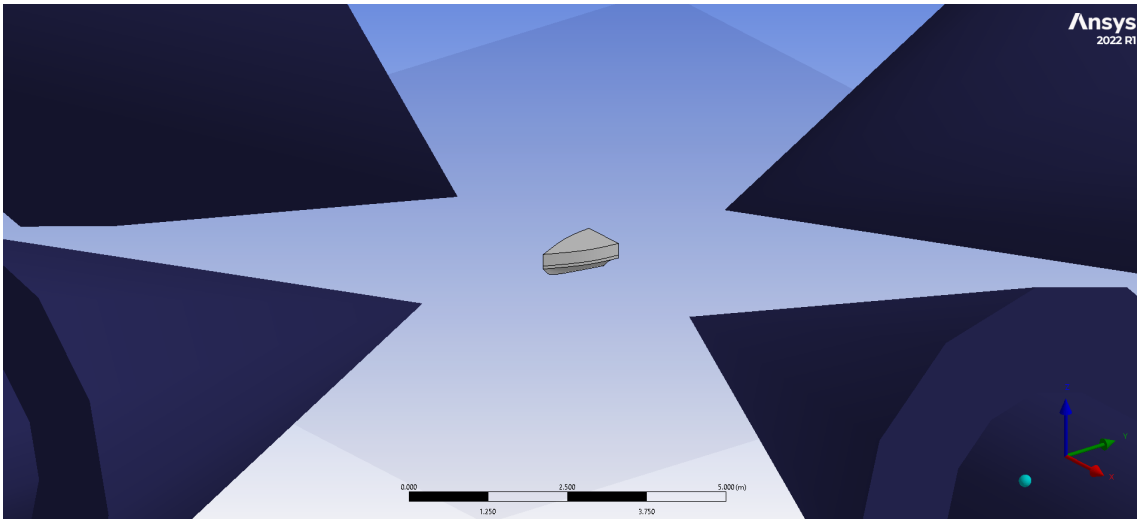

Figure 3.2: The environment setup of the BEM solver

At the beginning of the modeling and simulation, various mesh sizes have been tested. A finer mesh is more accurate, but it also takes longer time to simulate. Therefore, a reasonable mesh size that can be simulated in a short time meanwhile not sacrificing the accuracy of the simulation should be chosen at the start of the study. The mesh sizes tested in this study

include 0.02m, 0.025m, 0.03m, 0.04m and 0.05m as shown in the Fig. 3.3.

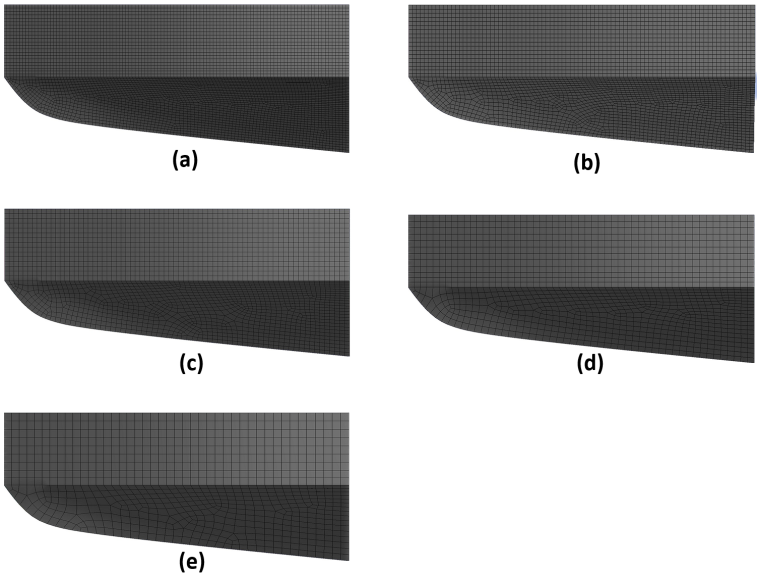

Figure 3.3: A buoy mesh side view at mesh size of (a) 0.02m; (b) 0.025m; (c) 0.03m; (d) 0.04m; (e) 0.05m;

With different mesh size, the BEM simulation results and simulation time are shown in the Fig. 3.4 and Table 3.1. From the Fig. 3.4, the added mass and excitation force values are slightly different at different mesh size, but the maximum difference is less than 1%. However, Table 3.1 shows a significant improvements of using mesh size larger than 0.03m on simulation time. Considering the large number of samples that are required for having simulations, a mesh size of 0.03m is chosen, which reduces the computational time by 70% more comparing to a finer mesh size meanwhile keeps a high accuracy of simulation results. Fig. 3.5 shows the pressure distribution of the wave on the buoy at wave height of $0.5m$ and wave period of $6sec$.

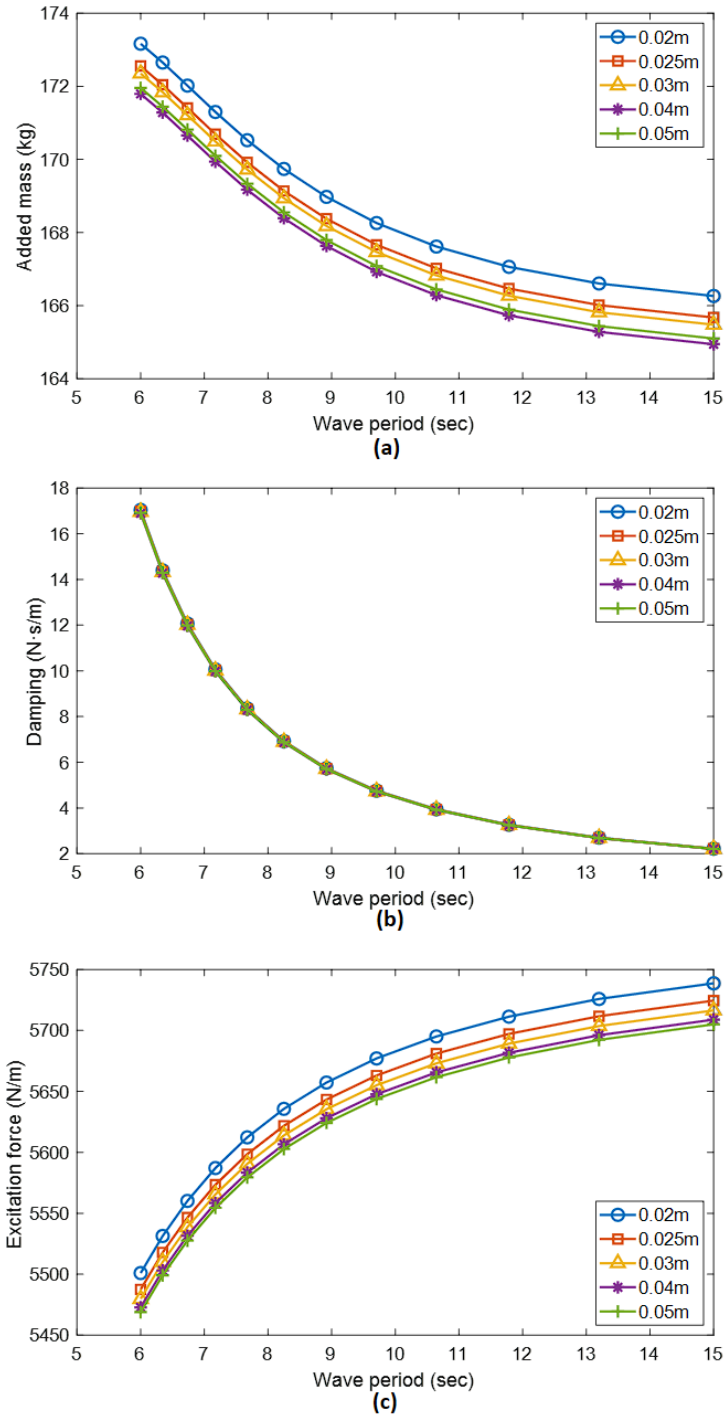

Figure 3.4: Simulated hydrodynamic parameters at different mesh size, including (a) added mass; (b) damping; (c) excitation force

Table 3.1: Simulation time using BEM software at different mesh size

Mesh size (m)	Time (sec)
0.02	289
0.025	166
0.03	45
0.04	37
0.05	22

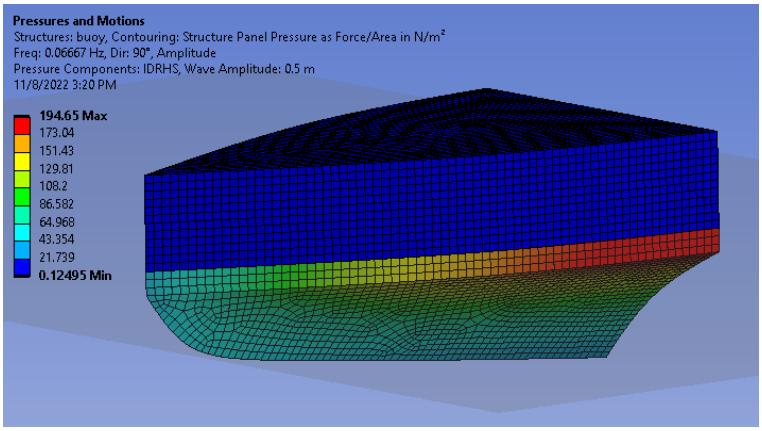

Figure 3.5: Pressure distribution of the wave on the buoy at wave height of $0.5m$ and wave period of $6sec$

3.2 Current Drag Force Modeling

In the ship hull design, reducing the ship resistance by solving for a optimal ship hull is one of the major objectives. Here, the current drag acting on the boat-shaped buoy is formulated in the same way as the ship resistance. The total resistance (F_D) is a combination of viscous resistance (F_V) and wave-making resistance (F_W) as shown in Eqn. (3.7) [47].

$$F_D = F_V + F_W \tag{3.7}$$

where, the formulations of F_V and F_W are [47] :

$$F_V = \frac{1}{2}\rho v^2 C_v S \tag{3.8}$$

$$F_W = \nabla \rho g \cdot f\left(F_r, \frac{L}{B}, T\right) \tag{3.9}$$

Here, ρ is water density, v is flow speed, C_v is coefficient of viscous resistance, S is underwater surface area, f represents a empirical function , ∇ is the total underwater volume, g is gravitational acceleration, F_r is froude number, L is buoy length, B is the buoy width and T is the draft (or ship depth).

In this study, considering the constraints mentioned in section 2.3, the viscous resistances F_V between different buoy shapes changed minimally due to extremely small changes in C_v and S are extremely small. Meanwhile, the underwater volume ∇, froude number F_r, buoy length L and draft T remain the same.

Therefore, the total resistance F_D now is only related to buoy width. To derive the function and understand the relationship between drag and buoy width, 20 boat-shaped buoys, with varying widths, are simulated using Computational Fluid Dynamics (CFD) solvers.

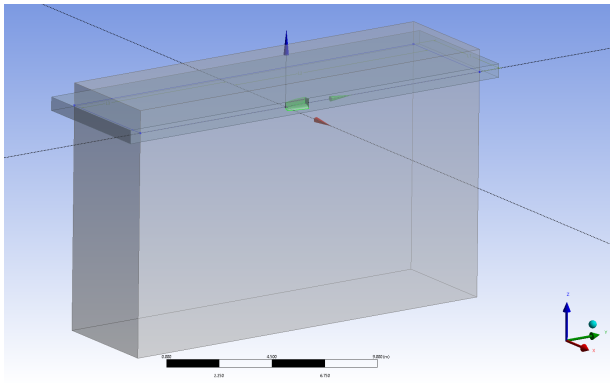

Figure 3.6: Drag simulation environment setup

Fig. 3.6 shows the CFD solver environment setup, which dimension is $10m \times 10m \times 10m$ $(L \times W \times D)$. The mesh result is shown in the Fig. 3.7, which has a mesh size of $0.04m$ for the outer area, and a mesh size of $0.02m$ for the inner area. The fluid model used in this study is the k-epsilon model [48] and the flow speed is set to be $2m/s$. Fig. 3.8 shows the residual plot and drag performance plot of the CFD simulation.

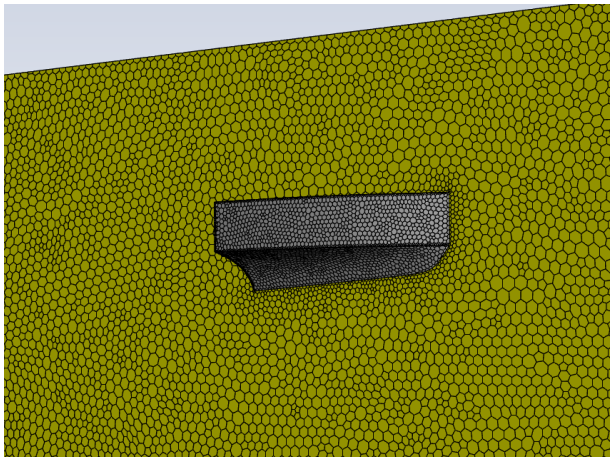

Figure 3.7: Mesh of the buoy for CFD simulation

Fig. 3.9 shows all simulated results from CFD, and a linear function is adopted to describe the relationship between buoy width and numerical drag for this study, which can be expressed as:

$$F_D = \alpha B - \beta \tag{3.10}$$

where, $\alpha = 312.58$ and $\beta = 31.39$ in this study.

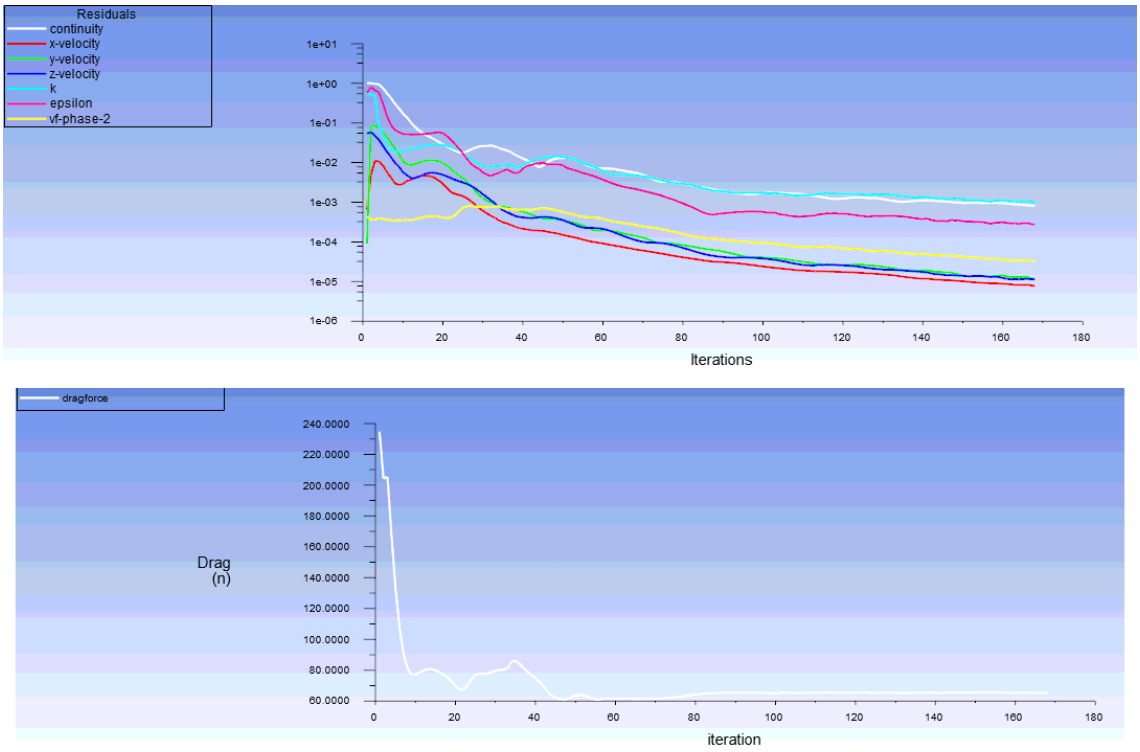

Figure 3.8: Residual plot and drag performance plot of the simulation

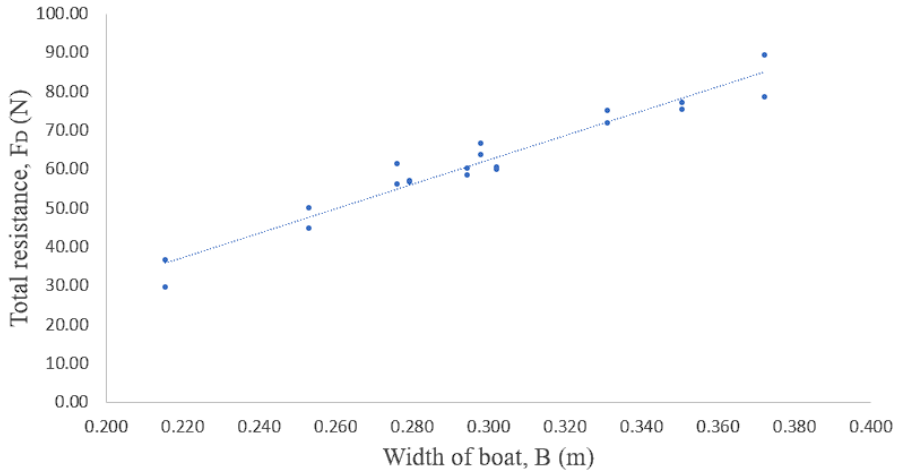

Figure 3.9: Total resistance (or drag force) on buoy at different width of the boat-shaped buoy

Chapter 4

Neural Network Model

This Chapter introduces the neural network model built in this study, which is able to replace the BEM and CFD solver and reduces the computational time from minutes to milliseconds. The structure of the neural network model applied in this works is a feed-forward neural network (FFNN) that has been developed for decays [49]. The construction of the neural network and the validation test results are discussed in this Chapter.

4.1 Feedforward Neural Network Construction

To calculate the power absorbed from the wave, the hydrodynamic parameters are required as shown in the Eqn. (3.1). These frequency dependent terms can be calculated using a BEM solver. Depending on the mesh size and the number of frequency intervals, the simulation takes from 30 seconds to more than 15 minutes with a AMD Ryzen 7 3800X 8-Core Processor. In this study, the maximum mesh size was chosen to vary from 0.02m to 0.05m, and the frequency intervals are set to 10, which takes 5 minutes for each simulation. Since the hydrodynamic parameters are mainly affected by the shape of the buoy, these parameters should be calculated in BEM solvers for each iteration during the optimization process. To reduce the computational time, a neural network model is trained to replace BEM solvers. The input of the neural network is set to be the parameter vector s in section 2.3 that represent the buoy shape and the output is the corresponding hydrodynamic parameters.

With a well trained neural network model, the output should be able to be calculated in milliseconds.

Fig. 4.1 shows a feed-forward neural network model that was applied in this study. The model was constructed with a input layer, multiple hidden layers, a output layer and a target value layer. The input layer includes the buoy shape parameter vectors while the target value layer records the hydrodynamic parameters (A_{11},c_{11}, and F_{e1}) from the samples data set. The hidden layers and output layer are calculated with Eqn.(4.1) and (4.2).

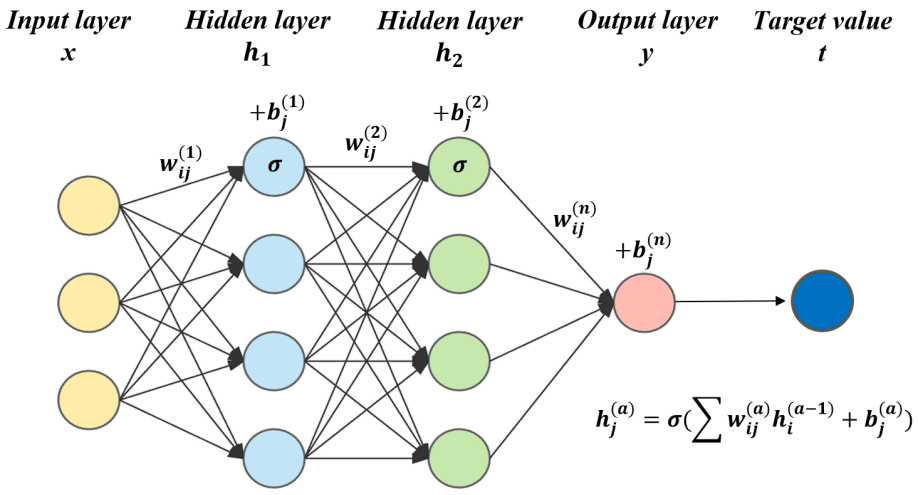

Figure 4.1: Neural network structure

$$h_j^{(a)} = \sigma\left(\sum w_{ij}^{(a)} h_i^{(a-1)} + b_j^{(a)}\right) \tag{4.1}$$

$$\sigma(\theta) = tansig\,(\theta) = \frac{e^{\theta} - e^{-\theta}}{e^{-\theta} + e^{\theta}} \tag{4.2}$$

Where, $h_j^{(a)}$ is the j-th neuron value at the a-th layer; $w_{ij}^{(a)}$ is the weight of the j-th neuron at the a-th layer from the i-th neuron at the $(a-1)$-th layer; $h_i^{(a-1)}$ is the i-th neuron value at the $(a-1)$-th layer; $b_j^{(a)}$ is the bias of the j-th neuron at the a-th layer. σ is the tan-sigmoid transfer function that has widely used in the neural network [50]. During the

training process, $w_{ij}^{(a)}$ and $b_j^{(a)}$ are updating, so that the output layer values can get closer to the target value.

4.2 Neural Network Training

Because the parametric model in this study is new, no previous studies have a sample data set that can be used to train the proposed neural network model. Therefore, a data set that includes 2400 buoy shapes parameter vectors and the corresponding hydrodynamic parameters is built. The automation codes, that generate 2400 random shapes in parameter vector form, import shapes into BEM simulation and save the hydrodynamic parameters results, have been uploaded to Github.

Fig. 4.2 shows one of the training process taking by the Matlab. The input layer has 12 parameters, and the output layer and target layer have 3 parameters. The training algorithm used in this study is the Matlab built-in bayesian regularization algorithm, which is one of the most popular training algorithms [51]. The loss function used in this study is the mean-squared-error (MSE) function shown in Eqn. 4.3.

$$MSE = \sum_{i=1}^{R} \frac{(t_i - y_i)^2}{R} \tag{4.3}$$

where, t_i is the target layer value; y_i is the output layer value; R is the total number of responses.

With the prepared 2400 shapes and their corresponding hydrodynamic parameters, the neural network model is ready to be trained. The Matlab built-in training function, Bayesian regularization backpropagation, is chosen to be the training algorithm. Table 4.1 shows the effect of the number of hidden layers and neurons on the accuracy of the neural network

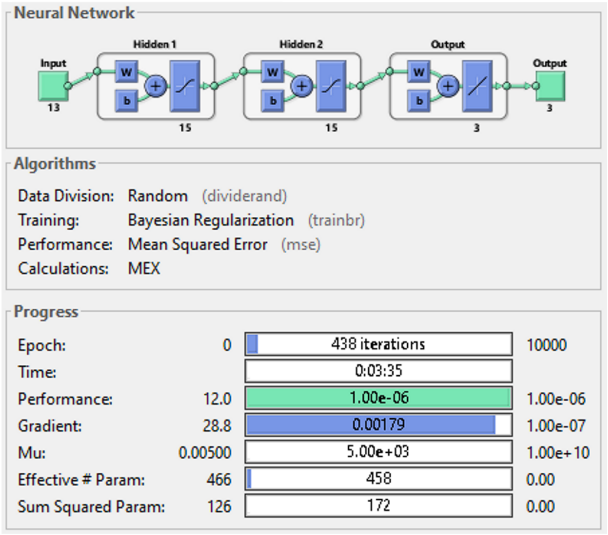

Figure 4.2: Neural network training using Matlab

model. With 2 hidden layers and 15 neurons, the model performs the best with a maximum training error of 1.2%.

Table 4.1: Neural network performance with various hidden layers and neurons

No. of hidden layers	No. of neurons	Max error (%)
1	5	20.7
1	10	9.3
1	15	3.1
2	5	12.8
2	10	5.5
2	15	1.2

4.3 Neural Network Validation

To ensure the neural network model isn't under-fitting or over-fitting, a validation test has been done with 100 new and random buoy shapes, which are outside the data set constructed in section 2.3. Fig. 4.3 compares the neural network results to the BEM simulation results.

For all three hydrodynamic parameters, the differences between neural network outputs and BEM outputs are extremely small. In order to see the difference more clearly, Fig. 4.4 plots the error difference between neural network results and the BEM results, where the error is calculated as:

$$Error = \frac{BEMResults - NeuralNetworkResults}{BEMResults} * 100\% \tag{4.4}$$

The figure indicates that the maximum error is less than 0.5%. Therefore, the neural network model is well-trained.

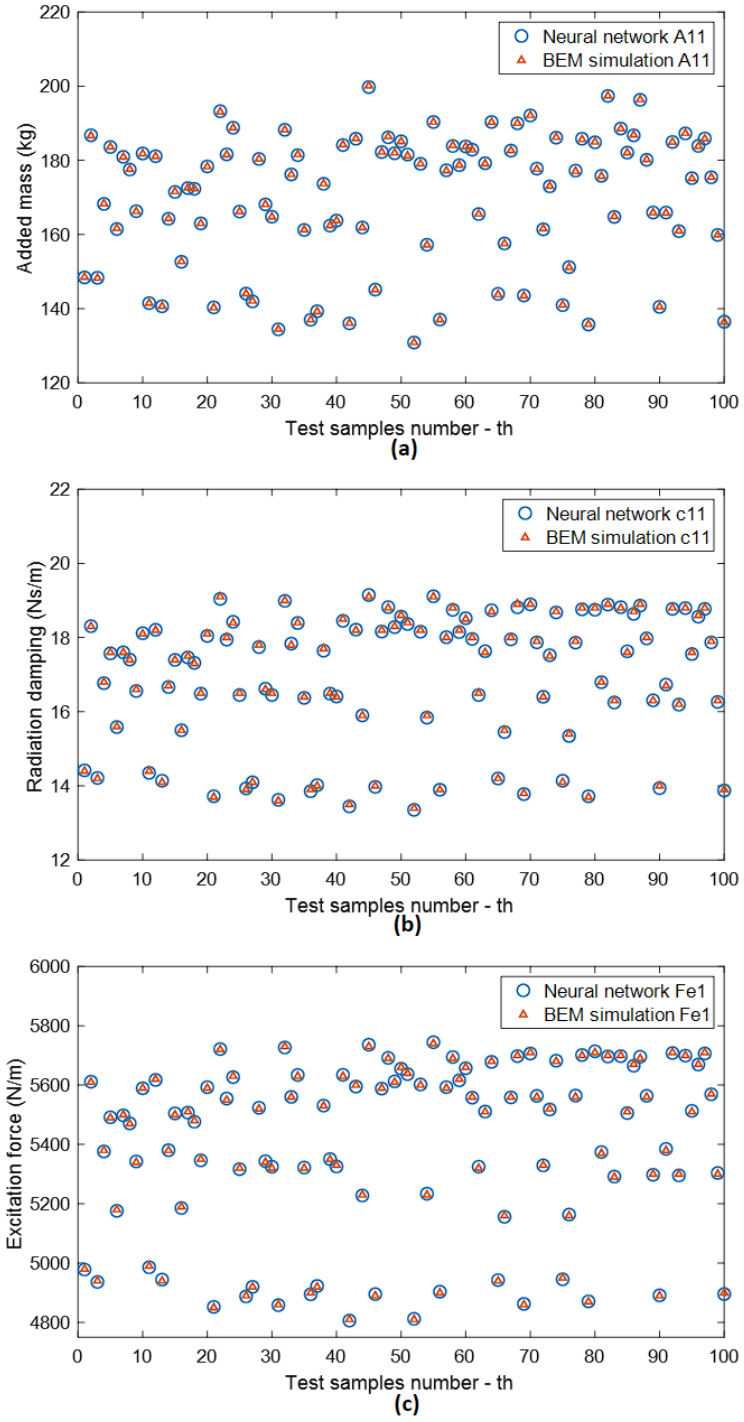

Figure 4.3: Validation results of 100 new buoy shapes at wave period = 6 sec and wave height = 0.5m. (a) Added mass results; (b) Radiation damping results; (c) Excitation force results

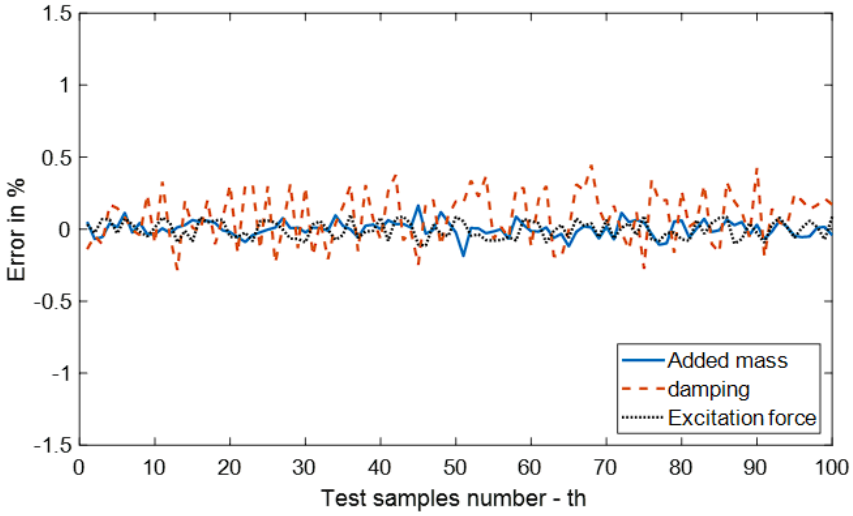

Figure 4.4: Validation test of difference in % between BEM solver outputs and neural network outputs

Chapter 5

Optimization using Genetic algorithm (GA)

In this Chapter, the application of GA in this study is presented. A self-developed algorithm and its flowchart are shown in the following sections. By adding multiple constraints checks, the new algorithm is able to search all cases mentioned in section 2.3. With the updated GA, the optimal boat-shaped buoy is solved successfully and comparing to the state-of-arts buoy shapes.

5.1 Introduction

GA is an algorithm that inspired by the species evolution. It starts with a population that includes a set of chromosomes. Then, it evaluates the score of each chromosome and ranks them in an order. The function that calculates the score is called "fitness function", and each value in a chromosome is called "gene". The chromosomes are called "parents" at the beginning of the iteration. Then, the "parents" that have high scores are selected to go through the crossover and mutation function. Fig. 5.1 shows an schematic of the crossover function with one crossover point and two crossover points. And Fig. 5.2 shows a schematic of the mutation function with the first gene mutated. The new chromosomes that generated by the crossover and mutation functions are called "offspring". Then, after an iteration

checks, the "parents" and "offspring" are combined into a new population, scored by the fitness function and go through the rest of the functions again.

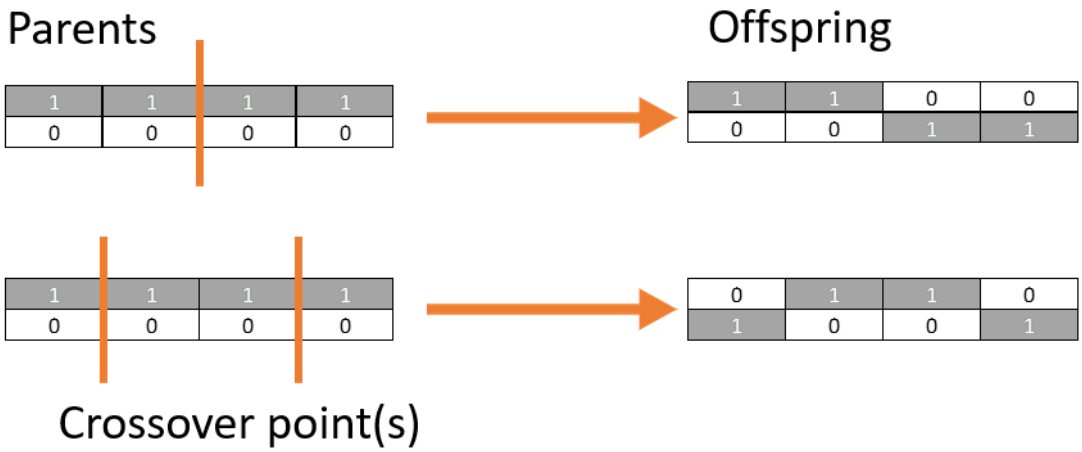

Figure 5.1: A schematic of the crossover function with one crossover point (top) and two crossover points (bottom)

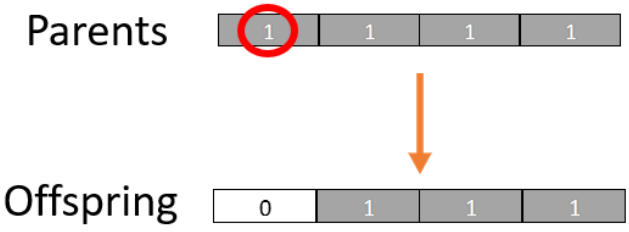

Figure 5.2: A schematic of the mutation function with one gene mutated

Fig. 5.3 shows a traditional GA flowchart which includes: generate initial population, calculate fitness of individuals, make selection, crossover, mutation and check stopping criteria.

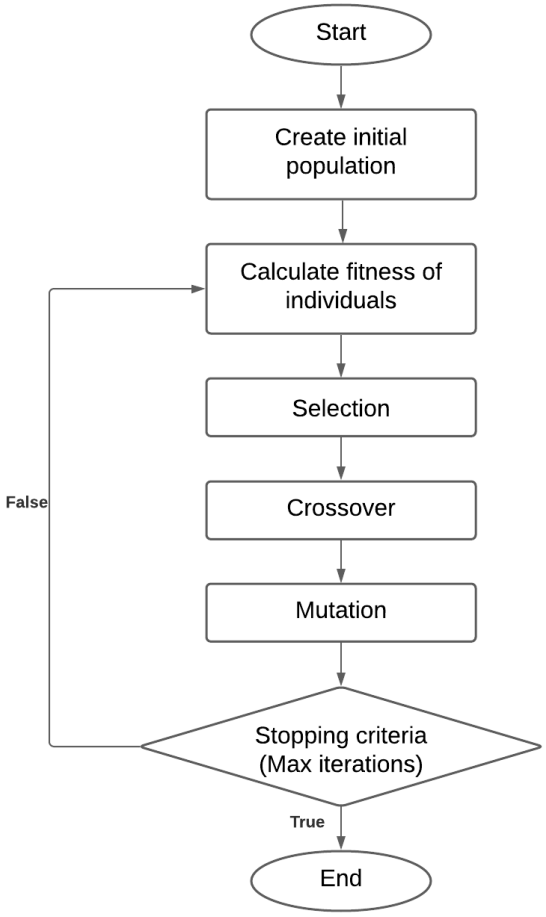

Figure 5.3: Traditional GA flowchart

5.2 Flowchart and Objective Function

Due to the complexity of the constraints mentioned in Eqn. (2.9) to (2.12), the traditional built-in GA function is unable to find the results. Therefore, a GA function designed for this problem is developed with an updated version of flowchart shown in Fig. 5.4, which checks the nonlinear constraints mentioned in section 2.3 after each crossover and mutation step.

Eqn.(5.1) shows the objective function, which is a score of the summation of the normalized absorbed power and the normalized current drag force. The weights of power and drag that

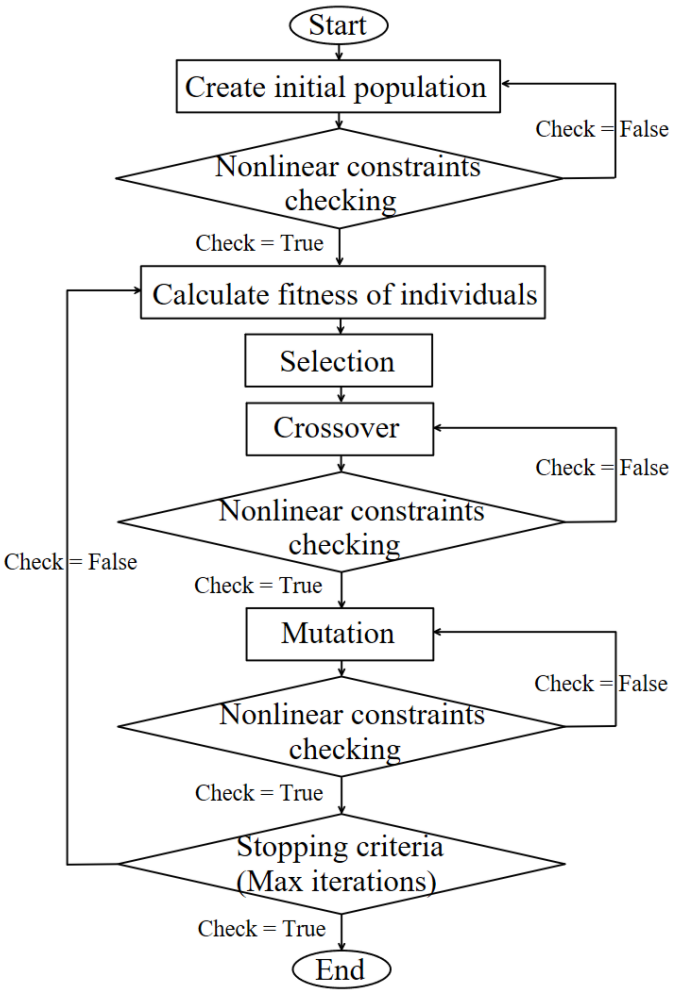

Figure 5.4: Updated GA flowchart

contribute to final score can be manually controlled depending on what is desired. In this study, w_1 is set to be 0.5, which means that the power and drag are considered equally important to the score. Several single objective GA optimizations are completed before the multi-objective task starts, to solve for the maximum and minimum power and drag values.

$$
\begin{aligned}
&maximize \quad J = w_1 f_1 + (1 - w_1) f_2 \\
&f_1 = \frac{P(s) - P_{min}}{P_{max} - P_{min}} \\
&f_2 = \frac{F_{max} - F(s)}{F_{max} - F_{min}}
\end{aligned}
\tag{5.1}
$$

where, J represents the objective function; f_1 is the normalized power; f_2 is the normalized drag; w_1 is the weight of the f_1; $P(s)$ and $F(s)$ is the wave power extraction estimated by the power model and the total current drag force model built in section 2.3; s is the shape vector built in section 2.3; P_{max},P_{min},F_{max},F_{min} are the maximum and minimum power and drag values in the search space.

5.3 Crossover and Mutation function

The crossover function and mutation function are two main functions that bring GA high diversity and allow GA jump out of the local minimum or maximum positions. Because the definition of the shape vector s (or chromosome in GA) is the combination of the outter deck, keel and ribs of the buoy, it is unreasonable to choose the crossover points and mutating gene randomly. Therefore, in this study, new methods of choosing crossover points and mutating gene are presented in Fig. 5.5 and Fig. 5.6.

where, x, k, r_x, r_y represent the outer deck s_x, keel s_y and ribs s_r of the first parent, where the definition of s_x, s_y, s_r can be found in Chapter 3; X, K, R_X, R_Y represent s_x, s_y, s_r of the second parent; α_1, α_2 are random values from 0 to 1; the offspring can be calculated using the equations in Fig. 5.5.

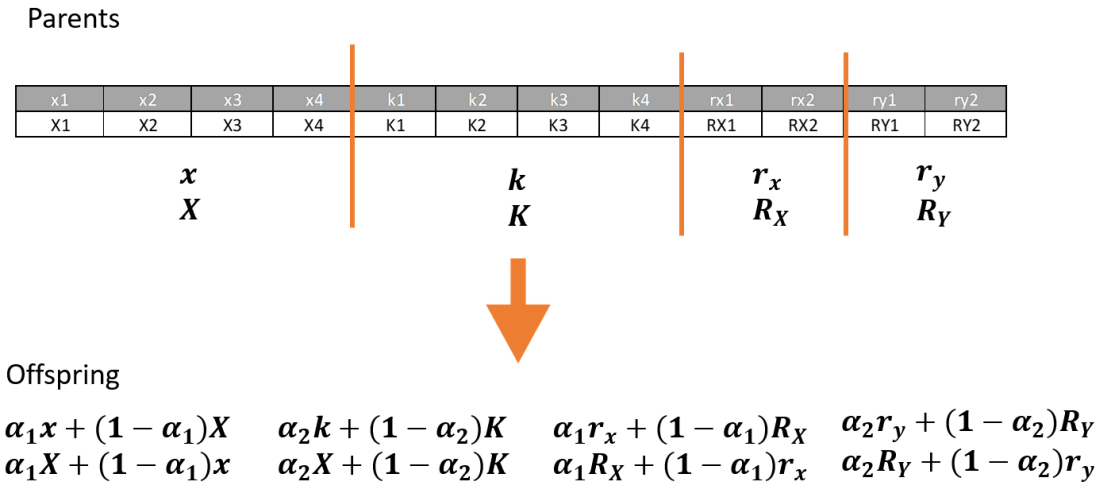

Figure 5.5: A schematic of the updated crossover function with crossover points distributed for outer deck, keel and ribs respectively

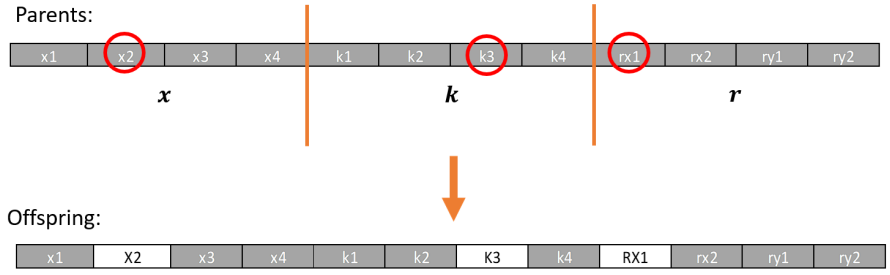

Figure 5.6: A schematic of the updated mutation function with one gene mutated for outer deck, keel and ribs respectively

5.4 GA Optimization Results and Validations

Fig. 5.7 shows the optimization track of 500 iterations, and the score increases from 54.2 to 65.8. Here, Fig. 5.8(a) shows the optimal boat-shaped buoy that constructed by the shape vector s solved by the GA. To validate the result, Table 5.1 compares the power and drag solved using neural network model and drag model developed in this study to the simulated results solved using BEM and CFD simulation tools. The drag differences between estimated

and simulated results are less than 10%, and the power differences are less than 1%.

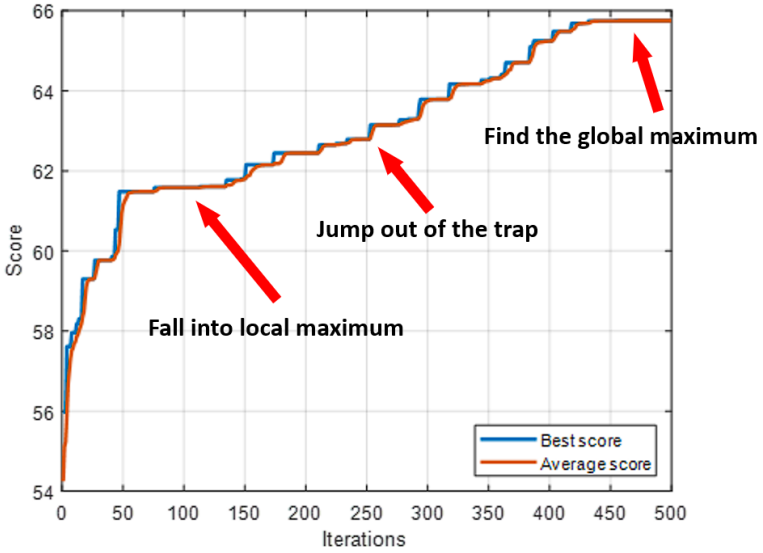

Figure 5.7: Optimization score

Table 5.1: Validation results between drag/power model and the CFD/BEM solver

Drag/Power Outputs Estimated by	Values
Linear drag model	48.3 N
CFD solver	52.0 N
Neural network power model	92.7 W
BEM solver	93.2 W

5.5 State-of-arts Buoys Comparison

A cylinder-shaped buoy and a thin-ship-shaped buoy (Fig. 5.8(b) and (c)) are chosen to compare to the optimal boat-shaped buoy. The cylinder-shaped buoy is one of the most common floating body of the point absorber typed wave energy converter [52]. And the thin-ship-shaped buoy is a scaled down yacht shape from Bašić et al. [52].

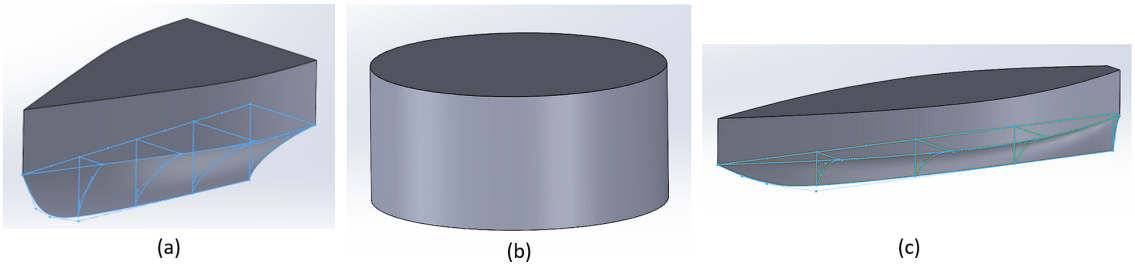

Figure 5.8: (a) Optimal boat-shaped buoy; (b) Cylinder-shaped buoy; (c) Thin-ship-shaped buoy

The comparison is done under the conditions of: same mass, same underwater volume, same cross-sectional area at waterline. As shown in Fig. 5.9, the optimal boat-shaped buoy reduces 68.7% of the current drag and has same level of power absorption compared to the cylinder-shaped buoy. Meanwhile, the optimal buoy increases 46.1% of power absorption and 33.3% of current drag compared to the thin-ship-shaped buoy. The optimal boat-shaped buoy performs much better on both current drag force reduction and wave power extraction side compared to the cylinder-shaped buoy and thin-ship-shaped buoy. One key point is that, all these conclusions are made under multiple conditions and constraints. For example, the wave and current interactions are ignored; only heave and surge directions system dynamics are considered; the ocean conditions are set to be under regular wave conditions, while the real ocean is irregular wave. However, this study is still meaningful on developing a new method to optimize the floating body of an ocean wave energy converter, which is much faster than using traditional BEM and CFD solvers. And we would like to consider more parameters and dimensions in the system modeling in the future studies.

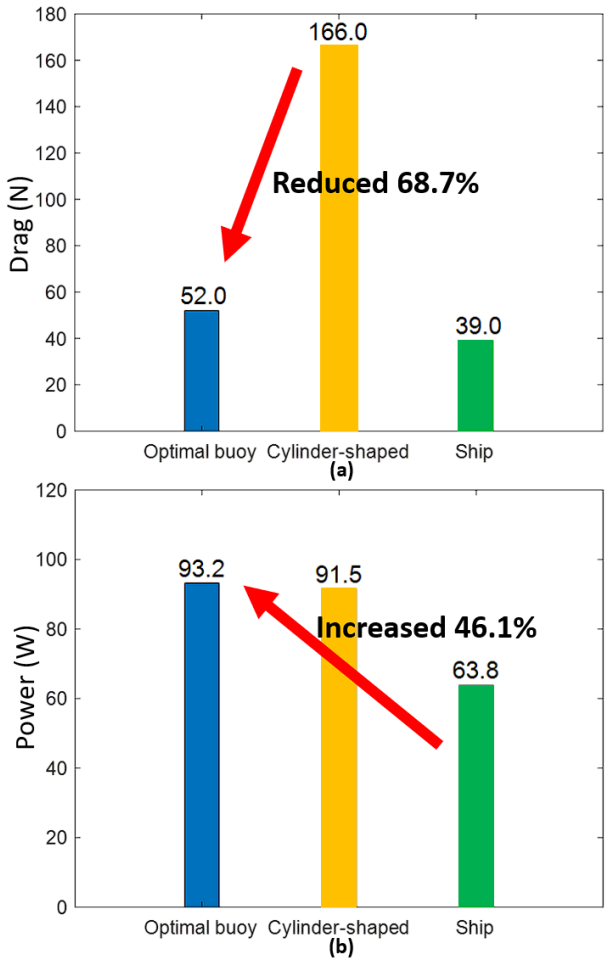

Figure 5.9: (a) Comparison of drag acting on the optimal boat-shaped buoy, cylinder-shaped buoy and thin-ship-shaped buoy under 2m/s flow speed condition. (b)Comparison of power extraction using optimal boat-shaped buoy, cylinder-shaped buoy and thin-ship-shaped buoy under wave period = 6 sec and wave height = 0.5m condition.

Chapter 6

Conclusion

In this study, a new method of optimizing the geometry of the buoy is developed, which enables the buoy having a shape to meet multiple objectives of wave capture and drag reduction. With the new parametric model, the shape of the buoy is controlled by 12 parameters, including 4 on the outer-deck, 4 on the keel and 4 on the rib. A neural network model is built to replace the traditional BEM software, which reduces the computational time for each iteration from minutes to milliseconds. A GA with multiple self-defined functions is developed to find the optimal shape of the buoy that meets the objective of maximizing power while minimizing the current drag.

Using the GA, the optimal boat-shaped buoy is solved after 500 iterations. The optimization results are compared to the direct BEM and CFD simulation results for validation. The drag force has a 10% difference while the power difference is less than 1% compared to the direct simulation results, which is acceptable. The optimization results show that the optimal boat-shaped buoy reduces 68.7% of current drag compared to a cylinder-shaped buoy, while having the same amount of power output absorbed through heave motion. Compared to a thin-ship-shaped buoy, the power absorption is increased by 46.1%, and the drag is also increased by 33.3%.

In conclusion, the new parametric model, neural network model and GA work well and can solve for an optimal shape of buoy with 12 parameters, with lower computational cost by more than 10,000 times compared to the traditional BEM and CFD methods. Further studies will

include but are not limited to: building a new drag model that can predict the current drag more accurate; expanding the optimization search space, such as enabling having different length of buoy and under irregular wave conditions; considering the wave-drag interaction influence; validating the results with tank test instead of pure simulation.

Bibliography

[1] Levi Kilcher, Michelle Fogarty, and Michael Lawson. Marine energy in the united states: An overview of opportunities. 2021.

[2] António F. de O. Falcão. Wave energy utilization: A review of the technologies. *Renewable and Sustainable Energy Reviews*, 14(3):899–918, 2010. ISSN 1364-0321. doi: https://doi.org/10.1016/j.rser.2009.11.003.

[3] Aqua-RET Project. Wave technology types. 2012.

[4] Boxi Jiang, Xiaofan Li, Shuo Chen, Qiuchi Xiong, Bang-fuh Chen, Robert G Parker, and Lei Zuo. Performance analysis and tank test validation of a hybrid ocean wave-current energy converter with a single power takeoff. *Energy Conversion and Management*, 224: 113268, 2020.

[5] Griet De Backer. Hydrodynamic design optimization of wave energy converters consisting of heaving point absorbers. *Department of Civil Engineering, Ghent University: Ghent, Belgium*, 2009.

[6] Ossama Abdelkhalik, Ryan G Coe, Giorgio Bacelli, and David G Wilson. Wec geometry optimization with advanced control. 57786:V010T09A031, 2017.

[7] Kai Zhu, Hongda Shi, Meng Han, and Feifei Cao. Layout study of wave energy converter arrays by an artificial neural network and adaptive genetic algorithm. *Ocean Engineering*, 260:112072, 2022.

[8] Liang Li, Zhen Gao, and Zhi-Ming Yuan. On the sensitivity and uncertainty of wave

energy conversion with an artificial neural-network-based controller. *Ocean Engineering*, 183:282–293, 2019.

[9] Austin Kyle Shaeffer, Wesley Wilson, and Chi Yang. Application of machine learning to early-stage hull form design. In *SNAME Maritime Convention*. OnePetro, 2020.

[10] Carlos VC Weiss, Raúl Guanche, Bárbara Ondiviela, Omar F Castellanos, and José Juanes. Marine renewable energy potential: A global perspective for offshore wind and wave exploitation. *Energy conversion and management*, 177:43–54, 2018.

[11] Sara Oliveira-Pinto, Paulo Rosa-Santos, and Francisco Taveira-Pinto. Assessment of the potential of combining wave and solar energy resources to power supply worldwide offshore oil and gas platforms. *Energy Conversion and Management*, 223:113299, 2020.

[12] Johannes Falnes. A review of wave-energy extraction. *Marine structures*, 20(4):185–201, 2007.

[13] Dongsheng Qiao, Rizwan Haider, Jun Yan, Dezhi Ning, and Binbin Li. Review of wave energy converter and design of mooring system. *Sustainability*, 12(19):8251, 2020.

[14] TV Heath. A review of oscillating water columns. *Philosophical Transactions of the Royal Society A: Mathematical, Physical and Engineering Sciences*, 370(1959):235–245, 2012.

[15] Ross Henderson. Design, simulation, and testing of a novel hydraulic power take-off system for the pelamis wave energy converter. *Renewable energy*, 31(2):271–283, 2006.

[16] David Elwood, Solomon C Yim, Joe Prudell, Chad Stillinger, Annette Von Jouanne, Ted Brekken, Adam Brown, and Robert Paasch. Design, construction, and ocean testing of a taut-moored dual-body wave energy converter with a linear generator power take-off. *Renewable Energy*, 35(2):348–354, 2010.

[17] Jens Peter Kofoed, Peter Frigaard, Erik Friis-Madsen, and Hans Chr Sørensen. Prototype testing of the wave energy converter wave dragon. *Renewable energy*, 31(2): 181–189, 2006.

[18] J Weber, F Mouwen, A Parish, and D Robertson. Wavebob—research & development network and tools in the context of systems engineering. In *Proc. Eighth European Wave and Tidal Energy Conference, Uppsala, Sweden*, volume 8, pages 416–420, 2009.

[19] Kathleen Edwards, Mike Mekhiche, et al. Ocean power technologies powerbuoy®: system-level design, development and validation methodology. 2014.

[20] Trevor Whittaker, David Collier, Matt Folley, Max Osterried, Alan Henry, and Michael Crowley. The development of oyster—a shallow water surging wave energy converter. In *Proceedings of the 7th European wave and tidal energy conference*, pages 11–14, 2007.

[21] Eshwan Ramudu. Ocean wave energy-driven desalination systems for off-grid coastal communities in developing countries. In *2011 IEEE Global Humanitarian Technology Conference*, pages 287–289. IEEE, 2011.

[22] Jonas Sjolte, Christian McLisky Sandvik, Elisabetta Tedeschi, and Marta Molinas. Exploring the potential for increased production from the wave energy converter lifesaver by reactive control. *Energies*, 6(8):3706–3733, 2013.

[23] Thomas Boerner, Nigel Kojimoto, Bryan Murray, and Dan Petcovic. California wave power technologies open water demonstration-budget period 1 reports. 2019.

[24] Elie Al Shami, Ran Zhang, and Xu Wang. Point absorber wave energy harvesters: A review of recent developments. *Energies*, 12(1):47, 2019.

[25] Kjell Budal and Johannes Falnes. Proposals for conversion of the energy in ocean waves. 1974.

[26] K Budal and J Falnes. Optimum operation of improved wave-power converter. *Mar. Sci. Commun.;(United States)*, 3(2), 1977.

[27] Chiang C Mei. Power extraction from water waves. *Journal of Ship Research*, 20(02): 63–66, 1976.

[28] Chiang C Mei, Michael Aharon Stiassnie, and Dick K-P Yue. *Theory and Applications of Ocean Surface Waves: Part 1: Linear Aspects*. World Scientific, 2005.

[29] Wanan Sheng. Wave energy conversion and hydrodynamics modelling technologies: A review. *Renewable and Sustainable Energy Reviews*, 109:482–498, 2019.

[30] DV Evans and R Porter. Wave energy extraction by coupled resonant absorbers. *Philosophical Transactions of the Royal Society A: Mathematical, Physical and Engineering Sciences*, 370(1959):315–344, 2012.

[31] Dillon Martin, Xiaofan Li, Chien-An Chen, Krish Thiagarajan, Khai Ngo, Robert Parker, and Lei Zuo. Numerical analysis and wave tank validation on the optimal design of a two-body wave energy converter. *Renewable energy*, 145:632–641, 2020.

[32] Pengyuan Sun, Qiang Li, Hongzhou He, Hu Chen, Jun Zhang, Hui Li, and Dahui Liu. Design and optimization investigation on hydraulic transmission and energy storage system for a floating-array-buoys wave energy converter. *Energy Conversion and Management*, 235:113998, 2021.

[33] Zhenwei Liu, Xu Wang, Elie Al Shami, Nick J Baker, and Xueyu Ji. A study of a speed amplified linear generator for low-frequency wave energy conversion. *Mechanical Systems and Signal Processing*, 149:107226, 2021.

[34] John V Ringwood. Wave energy control: status and perspectives 2020. *IFAC-PapersOnLine*, 53(2):12271–12282, 2020.

[35] Shangyan Zou, Ossama Abdelkhalik, Rush Robinett, Giorgio Bacelli, and David Wilson. Optimal control of wave energy converters. *Renewable energy*, 103:217–225, 2017.

[36] Umesh A Korde and John Ringwood. *Hydrodynamic control of wave energy devices*. Cambridge University Press, 2016.

[37] Bingyong Guo and John V Ringwood. Geometric optimisation of wave energy conversion devices: A survey. *Applied Energy*, 297:117100, 2021.

[38] Jean-Christophe Gilloteaux and John Ringwood. Control-informed geometric optimisation of wave energy converters. *IFAC Proceedings Volumes*, 43(20):366–371, 2010.

[39] Pedro Jorge Borges Fontes Negrao Beirao and Cândida Maria dos Santos Pereira Malça. Design and analysis of buoy geometries for a wave energy converter. *International Journal of Energy and Environmental Engineering*, 5(2):1–11, 2014.

[40] Emma C Edwards and Dick K-P Yue. Optimisation of the geometry of axisymmetric point-absorber wave energy converters. *Journal of Fluid Mechanics*, 933, 2022.

[41] Xuanrui Huang, Kai Sun, and Xi Xiao. A neural network-based power control method for direct-drive wave energy converters in irregular waves. *IEEE Transactions on Sustainable Energy*, 11(4):2962–2971, 2020.

[42] PMR Bento, JAN Pombo, RPG Mendes, MRA Calado, and SJPS Mariano. Ocean wave energy forecasting using optimised deep learning neural networks. *Ocean Engineering*, 219:108372, 2021.

[43] Tomasz Abramowski. Application of artificial intelligence methods to preliminary design of ships and ship performance optimization. *Naval Engineers Journal*, 125(3):101–112, 2013.

[44] Tomasz Cepowski. The prediction of ship added resistance at the preliminary design stage by the use of an artificial neural network. *Ocean Engineering*, 195:106657, 2020.

[45] Les Piegl. On nurbs: a survey. *IEEE Computer Graphics and Applications*, 11(01): 55–71, 1991.

[46] Shahroz Khan, Erkan Gunpinar, and Kemal Mert Dogan. A novel design framework for generation and parametric modification of yacht hull surfaces. *Ocean Engineering*, 136:243–259, 2017.

[47] J Holtrop and GGJ Mennen. An approximate power prediction method. *International Shipbuilding Progress*, 29(335):166–170, 1982.

[48] Bijan Mohammadi and Olivier Pironneau. Analysis of the k-epsilon turbulence model. 1993.

[49] Daniel Svozil, Vladimir Kvasnicka, and Jiri Pospichal. Introduction to multi-layer feed-forward neural networks. *Chemometrics and intelligent laboratory systems*, 39(1):43–62, 1997.

[50] Thomas P Vogl, JK Mangis, AK Rigler, WT Zink, and DL Alkon. Accelerating the convergence of the back-propagation method. *Biological cybernetics*, 59(4):257–263, 1988.

[51] Frank Burden and Dave Winkler. Bayesian regularization of neural networks. *Artificial neural networks*, pages 23–42, 2008.

[52] A Garcia-Teruel and DIM Forehand. A review of geometry optimisation of wave energy converters. *Renewable and Sustainable Energy Reviews*, 139:110593, 2021.